## PAPER

Check for updates

# Structure and luminescence properties of Dy³⁺ doped quaternary tungstate Li₃Ba₂Gd₃(WO₄)₈ for application in wLEDs†

Abir Douzi,[ab] Sami Slimi, [ID][a] Eduard Madirov,[c] Andrey Turshatov, [ID][c] Bryce S. Richards, [ID][c] Rosa Maria Solé, [ID][a] Magdalena Aguiló,[a] Francesc Díaz,[a] Ezzedine Ben Salem[b] and Xavier Mateos [ID] *[a]

Quaternary tungstates with the composition Li₃Ba₂Gd₃(WO₄)₈ doped with different concentrations of Dy³⁺ (from 0.5 to 10 at%) were prepared by the solid-state reaction method at 900 °C. Their structural, spectroscopic and optical properties were studied systematically in this work. X-ray diffraction analysis confirmed the crystallization of Li₃Ba₂Gd₃(WO₄)₈ to have a monoclinic structure (sp. gr. *C2/c*); the lattice constants for 1 at% doping concentration of Dy³⁺ are $a = 5.2126(2)$ Å, $b = 12.7382(1)$ Å, $c = 19.1884(3)$ Å, $V_{calc} = 1273,40(4)$ Å³ and $\beta = a \times c = 91.890(9)°$. The first principles calculations for the undoped crystal revealed a direct bandgap of 2.45 eV, which is very close to the experimental one. The identified broad, and strong excitation peak at 450 nm indicates that Li₃Ba₂Gd₃(WO₄)₈:Dy³⁺ phosphors are suitable to be pumped by a blue laser diode (LD). Under excitation at 445 nm, the phosphor showed a stronger luminescence peak at 575 nm which corresponds to the Dy³⁺:⁴F₉/₂ → ⁶H₁₃/₂ transition, and three weaker emissions peaks at 477, 661, and 750 nm. Meanwhile, the effect of different Dy³⁺ contents on the luminescence properties was investigated. The optimum concentration to minimize the quenching effect was 4 at% and the critical distance is 31.209 Å. The phosphor emitted strong greenish-yellow light situated at (0.425, 0.472) in CIE coordinates with a color temperature of 3652 K. All the measured luminescence lifetime curves exhibited a single-exponential nature. Excellent thermal stability was found for this tungstate phosphor (the activation energy is 0.352 ± 0.01 eV). The measured absolute photoluminescence quantum yield was around 10.5%. The results presented in this work show that Li₃Ba₂Gd₃(WO₄)₈:Dy³⁺ phosphors with strong yellow emission are promising candidates for white-light emitting LED (wLED) applications.

## 1. Introduction

In recent years, white light-emitting diodes (wLEDs) in the field of solid-state lighting have gained growing attention due to their outstanding advantages, such as high reliability, high luminous efficiency, good material stability and environmental sustainability.[1–5] Presently, one of the most common approaches to achieve white light is to blend commercial blue LED chips with yellow phosphors such as the well-known Ce³⁺-doped yttrium aluminum garnet (YAG:Ce³⁺).[6,7] It shows high stability and performance (high PhotoLuminescence Quantum

Yield, PLQY), absorbing blue light and emitting yellow persistent luminescence, as well as combining efficiently those blue and yellow photons to yield white light in a compact wLED.[8] However, the YAG material has a high melting point (∼1970 °C[9]) which makes the industrial exploitation of this material expensive. It is therefore relevant to search for new effective luminescent materials that radiate yellow light with cheaper industrial fabrication cost (*e.g.* lower melting temperature). The performance of such wLEDs highly depends on the luminescence performance of the phosphors which are doped with different rare-earth ions (RE).[10,11] The host matrix and activator ions are two factors that influence the luminescence properties of the phosphor.

Among the activator ions (RE), dysprosium ions (Dy³⁺) are of interest to produce yellow emission. The ⁴F₉/₂ → ⁶H₁₅/₂ and ⁴F₉/₂ → ⁶H₁₃/₂ transitions in Dy³⁺ ions are located in the blue and yellow spectral regions, respectively. It is known that the ⁴F₉/₂ → ⁶H₁₃/₂ transition is hypersensitive to the crystal field (according to the selection rules $\Delta L = 2$, $\Delta J = 2$).[12–14] Therefore, the relative intensity of the yellow emission is responsive to the

*ᵃUniversitat Rovira i Virgili (URV, ), Física i Cristal lografia de Materials (FiCMA), Marcel·li Domingo 1, 43007, Tarragona, Spain. E-mail: xavier.mateos@urv.cat*

*ᵇI.P.E.I. of Monastir, Unit of Materials and Organic Synthesis, University of Monastir, 5019, Tunisia*

*ᶜInstitute of Microstructure Technology, Karlsruhe Institute of Technology, Hermann-von-Helmholtz-Platz 1, 76344 Eggenstein-Leopoldshafen, Germany*

surrounding local environment of the $Dy^{3+}$ ions and it is possible to change the ratio of yellow to blue (Y/B) emission intensities and produce white light using $Dy^{3+}$ doped luminophores.[15,16] The Y/B ratio depends on the level of $Dy^{3+}$ doping and the structure of the host matrix (*i.e.*, the symmetry of the point group for the $Dy^{3+}$ ion sites).[17] The emission intensity of the $^4F_{9/2} \rightarrow {}^6H_{13/2}$ transition is greater than that of the $^4F_{9/2} \rightarrow {}^6H_{15/2}$ transition (resulting in yellow luminescence) for the case where $Dy^{3+}$ ions localize to the low-symmetry sites, and *vice versa*. Among the many crystals that have been reported, tungstate crystals exhibit a much higher Y/B intensity ratio compared to other crystals, due to the high level of covalency of the metal–ligand binding.[18–20]

Tungstate crystals are an important class of oxide host matrix for doping with RE ions. These crystals have received much interest due to their stable chemical properties, rich crystal chemistry, and potential applications in areas such as laser systems, electrochemistry, and photonics.[21–23] As a member of the tungstate family of materials, the quaternary compound $Li_3Ba_2RE_3(WO_4)_8$ (RE = La–Lu, Y), which is isostructural with $Li_3Ba_2RE_3(MoO_4)_8$, has been explored as a host for solid-state lasers, and its crystal structure has been solved by Pan *et al.*[24,25] It shows a monoclinic system with $C2/c$ space group symmetry. Due to the occurrence of a statistical distribution of rare-earth and lithium atoms, these crystals exhibit high structural disorder, which results in homogeneous broadening of the absorption and emission lines when rare-earth ions are doped and fill the positions of $RE^{3+}$ ions.[26] So far, several studies were dedicated to $Li_3Ba_2RE_3(WO_4)_8$ type-phosphors for applications in wLED. $Li_3Ba_2Y_3(WO_4)_8$:$Tb^{3+}$/$Eu^{3+}$ emits white light, which is composed of three typical emission bands: green from $Tb^{3+}$, red from $Eu^{3+}$, and blue from the substrate. The luminescent colors can be tuned by adjusting the relative doping ratios of $Eu^{3+}$ and $Tb^{3+}$ in $Li_3Ba_2Y_3(WO_4)_8$ phosphor, resulting in changes in the spectral components.[27] Thus, $Li_3Ba_2Y_3(WO_4)_8$:$Eu^{3+}$ was synthesized by a high temperature solid-state reaction method. The color purity (97.2%) and thermal stability (activation energy $\Delta E = 0.27$ eV) were found to be better than that of the commercial $Y_2O_2S$:$Eu^{3+}$ phosphor.[28] For the past few years, less attention has been paid to isostructural Gd-based compounds, *e.g.*, lithium barium gadolinium quaternary tungstate $Li_3Ba_2Gd_3(WO_4)_8$. Few studies predicted the suitability of the single crystal $Li_3Ba_2Gd_3(WO_4)_8$ doped with $Nd^{3+}$ (ref. 29) and $Yb^{3+}/Er^{3+}$ (ref. 30) for application in diode pumped lasers. Guo *et al.* reported on the characteristic of the green emission with high color purity collected from the phosphor $Li_3Ba_2Gd_3(WO_4)_8$:$Tb^{3+}$.[31] Nevertheless, to the best of our knowledge, based on this tungstate host, the preparation of new types of phosphors for solid-state lighting is still relatively rare.
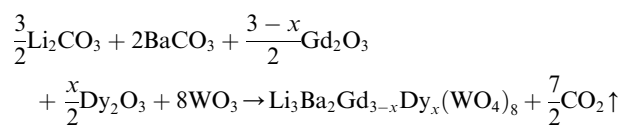
Herein, in this work, new $Dy^{3+}$ ions-doped $Li_3Ba_2Gd_3(WO_4)_8$ phosphors have been successfully synthesized by the conventional solid-state method. The structural, morphological, photoluminescence, and colorimetric properties were discussed in detail to yield that the $Li_3Ba_2Gd_3(WO_4)_8$:$Dy^{3+}$ is a promising yellow light emitting phosphor for solid-state lighting applications.

# 2. Experimental and methods

## 2.1. Materials synthesis

A new family of tungsten, $Li_3Ba_2Gd_3(WO_4)_8$ doped with $Dy^{3+}$ was synthesized using the traditional solid-state reaction method to explore and develop new phosphors. $Li_2CO_3$ (>99%, VWR Chemicals), $BaCO_3$ (99.9%, chemPUR), $Gd_2O_3$ (99.99%, Treibacher AG), $Dy_2O_3$ (99.99%, Treibacher AG) and $WO_3$ (99.9%, Honeywell Fluka) were used as reagents. They were first weighed in stoichiometric proportions, then transferred with ethanol to an agate mortar and carefully ground for 2 h to obtain a homogeneous mixture. After complete evaporation of the alcohol, they were placed directly into an alumina crucible, placed in a muffle furnace and sintered at 700 °C for one day in air to remove the $CO_2$. Then, to obtain single-phase samples of $Li_3Ba_2Gd_{3-x}Dy_x(WO_4)_8$ ($x$ being from 1 at% to 10 at% in the raw materials mixture) we had to repeat the process again but keeping the temperature at 900 °C to achieve the pure phase while handling the mixture comfortably without melting. This was in air atmosphere for 24 h to ensure the adequate chemical reaction.

The $Li_3Ba_2Gd_{3-x}Dy_x(WO_4)_8$ samples were prepared using the following chemical reaction:

$$\frac{3}{2}Li_2CO_3 + 2BaCO_3 + \frac{3-x}{2}Gd_2O_3$$
$$+ \frac{x}{2}Dy_2O_3 + 8WO_3 \rightarrow Li_3Ba_2Gd_{3-x}Dy_x(WO_4)_8 + \frac{7}{2}CO_2\uparrow$$

## 2.2. Experimental measurements

Structural characterization of the synthesized $Li_3Ba_2Gd_3(WO_4)_8$:$xDy^{3+}$ powders was performed by X-ray powder diffraction. Measurements were performed using a Bruker-AXS D8-Advance diffractometer with a vertical $\theta-\theta$ goniometer with Cu K$\alpha$ radiation (1.5406 Å). To detect the diffracted X-rays, a position sensitive detector (LynxEye-XE-T) was employed with an opening angle of 2.94°. For Rietveld refinement, the recording conditions were step size of 0.02° and step time of 2 s in the $2\theta$ range from 5° to 80°. The support of the sample was Si(510), which has low background. The Rietveld refinement was computed using GSAS II software.

The infrared (IR) spectra were recorded using a Fourier transform infrared spectrometer (FTIR, model FI/IR 6700, Jasco). Raman spectra were taken with a Renishaw InVia confocal Raman microscope that was equipped with an edge filter, a 50× objective, and an $Ar^+$ ion laser as the excitation source (with $\lambda_{ex} = 514$ nm). Differential thermal analysis (DTA) was performed using a MOM Q-1500 D derivatograph, using a Pt–Rh thermocouple and a Pt crucible. The heating and cooling rates were both 15 °C min$^{-1}$ and under 140 cm$^3$ min$^{-1}$ of nitrogen flow. The sample weight was 3.5 mg. The accuracy of the temperature measurement was approximately ±5 °C. The composition of the samples was determined using electron dispersive X-ray spectroscopy (EDX) and was performed using a FEI Quanta 600 environmental scanning electron microscope (SEM) connected to an microanalyzer (Oxford Inca 3.0).

A spectrophotometer (Varian Cary 5000 UV-visible-IR), equipped with an integrating sphere, was employed to record

the reflectance spectra at room temperature (RT, 20 °C) from 200 nm to 700 nm, on 12 mm diameter pellet samples, with a data interval of 0.5 nm and an integration time of 1 s. The photoluminescence (PL) spectroscopy under 445 nm excitation was performed using an in-house setup based on a diode laser (FC-445-2W) with a power of 1.1 W, coupled to an optical fiber and collimating lens to focus the light on the sample, and a spectral analyzer (OSA, Ando AQ6315-E) for detection. The excitation and emission (under $\lambda_{ex}$ = 350 nm) spectra were obtained using the spectrofluorometer (FS5, Edinburgh Instruments), with a built-in xenon lamp serving as the excitation source. PL lifetime measurements were performed using a photomultiplier tube (R928P, Hamamatsu), mounted in a temperature-cooling housing (CoolOne, Horiba), with the PLwavelength being selected with a double monochromator (Bentham, DTMS300). The excitation source was a 445 nm laser diode (Roithner) mounted in a temperature stabilized mount (TCLDM9, Thorlabs) and driven by a laser diode controller (ITC4001, Thorlabs). The photoluminescence quantum yield PLQY value is estimated with an optical setup built around an integrating sphere (Labsphere, 6″Ø, 3 P-LPM-060-SL). The sample is placed in the middle of a sphere and is excited with a CW LED operating at 445 nm (Thorlabs, M450LP2) that is driven with a laser diode controller (Thorlabs, ITC4001).

The theoretical calculations of energy band structures were carried out using the density functional theory (DFT) plane-wave pseudopotential method *via* the Cambridge Serial Total Energy Package (CASTEP) code.[32] The bandgap and electron structure of the host $Li_3Ba_2Gd_3(WO_4)_8$ were calculated using the Perdew–Burke–Ernzerhof function within the generalized gradient approximation. The crystal parameters were taken from ref. 29. For the Brillouin zone, the Monkhorst–Pack scheme $k$-points grid sampling was set at $5 \times 5 \times 5$, while a kinetic energy cutoff of 910 eV was used during calculations. The convergence tolerances of the maximum energy change, maximum force, and maximum displacement for the geometry optimization were $1.0 \times 10^{-5}$ Hartree, 0.03 Hartree $Å^{-1}$, and 0.001 Å, respectively. Pseudopotential = Norm conserving, FFT density = $54 \times 54 \times 144$, SCF tolerance = $10^{-5}$ eV per atom, Monkhorst-Pack grid = 1/0.03 Å $\times$ 1/0.03 Å $\times$ 1/0.03 Å, $k$ points set = 1/0.002 Å and the Brillouin zone path is: $L(-0.5, 0, 0.5) \rightarrow M(-0.5, 0.5, 0.5) \rightarrow A(-0.5, 0, 0) \rightarrow G(0, 0, 0) \rightarrow Z(0, -0.5, 0.5) \rightarrow V(0, 0, 0.5)$.

## 3. Results and discussion

### 3.1. Crystal structure analysis

The crystal structure and phase purity of the prepared powders were confirmed by XRD. Fig. 1(a) shows the XRD profiles of the prepared $Li_3Ba_2Gd_{3-x}(WO_4)_8$:$xDy^{3+}$ phosphors for $x$ in the range 0–10 at%. The relative intensity and position of the diffraction peaks of the synthesized powders are in good agreement with the JCPDS (Joint Committee on Powder Diffraction Standards) #7211787 for the 5 at% $Nd$:$Li_3Ba_2Y_3(WO_4)_8$ crystal displayed in Fig. 1(b). No other diffraction peaks from impurities are detectable, indicating that the prepared samples are single-phase. $Li_3Ba_2Gd_{3-x}(WO_4)_8$:$x$ at% $Dy^{3+}$ phosphors crystallize in the monoclinic class with the $C2/c$ space group ($2/m$ point



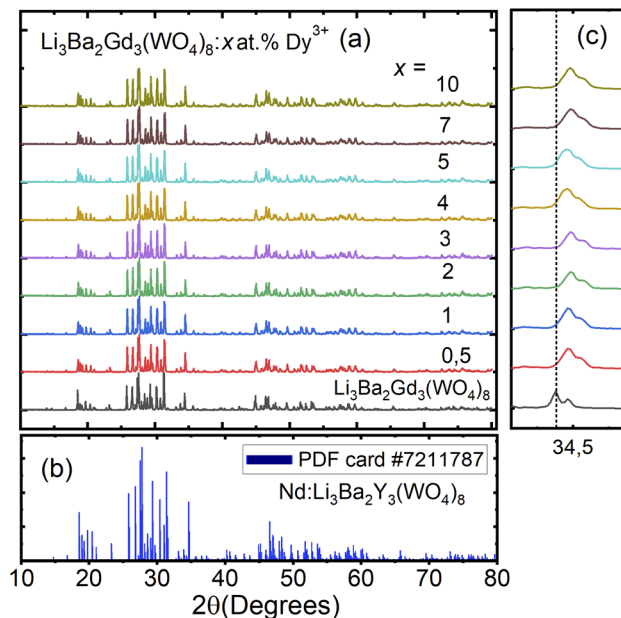**Fig. 1** (a) X-ray diffraction (XRD) patterns of $Li_3Ba_2Gd_3(WO_4)_8$ with different doping concentration of $Dy^{3+}$ ions (0–10 at%); (b) standard powder diffraction card of $Nd$:$Li_3Ba_2Y_3(WO_4)_8$, COD ID: 7211787; (c) deviation of the diffraction peak (200) as function of doping concentration.

group). The doping levels studied with $Dy^{3+}$ ions do not change the structure of the material (same monoclinic phase), although the positions of the XRD diffraction peaks slightly shift to higher angles with respect to the undoped sample (Fig. 1(c)). This, according to Bragg's law, indicates a change in lattice constants. In addition, the sharp and intense peaks indicate that the samples have high crystallinity, which is advantageous for improving the luminous efficiency of the phosphors. According to the Shannon reference, the ionic radii of $Dy^{3+}$, $Li^+$, $Ba^{2+}$ and $Gd^{3+}$ are as follows: $Dy^{3+}$ (1.027 Å, coordination number (CN) = VIIl), $Li^+$ (0.92 Å, CN = VIIl), $Ba^{2+}$ (1.42 Å, CN = VIIl) and $Gd^{3+}$ (1.053 Å, CN = VIIl).[33] It can be noted that $Gd^{3+}$ has the closest radius and has the same charge number as $Dy^{3+}$. The $Dy^{3+}$ ions in $Li_3Ba_2Gd_3(WO_4)_8$ are expected to replace the trivalent host-forming cations, $Gd^{3+}$, in the 8f site type. The replacement of $Gd^{3+}$ by $Dy^{3+}$ is expected to induce a change in the lattice parameters. Indeed, a decrease in lattice constants has been noticed previously. The replacement of $Gd^{3+}$ ions in the lattice by $Dy^{3+}$ is supported by the % difference in ionic radii ($D_r$) between the activator ($Dy^{3+}$) and the host ion ($Gd^{3+}$), determined using eqn (1):[34]

$$D_r = \frac{R_h(CN) - R_d(CN)}{R_h(CN)} \times 100\% \qquad (1)$$

where $R_h$, $R_d$, and CN represent the ionic radii of the host ion ($Gd^{3+}$), activator ion ($Dy^{3+}$), and coordination number, respectively. From the calculation, $D_r \sim 2.5\%$ for CN = VIIl, demonstrating the appropriate replacement of gadolinium by dysprosium in the crystal matrix. In order to better understand the structure of $Li_3Ba_2Gd_{3-x}(WO_4)_8$:$xDy^{3+}$ and the incorporation behavior of $Dy^{3+}$ ions into the $Li_3Ba_2Gd_{3-x}(WO_4)_8$ host matrix,
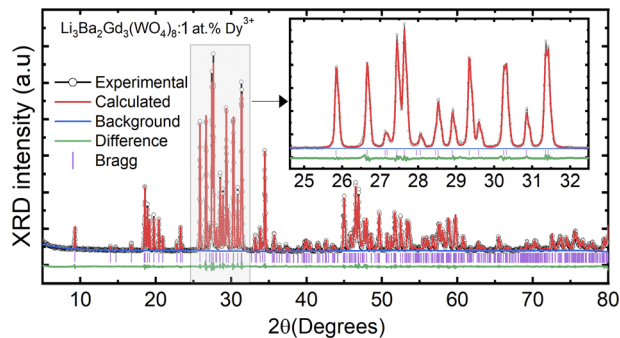
**Fig. 2** Rietveld refinement plots for $Li_3Ba_2Gd_3(WO_4)_8$: 1 at% Dy: the experimental profile-black line; the calculated pattern-red line; the difference plot-green line and the background-blue line; (Inset) zoomed view in the range between 25 and 32°.

**Table 1** Crystallographic data and Rietveld refinement details for $Li_3Ba_2Gd_3(WO_4)_8$: 1 at% $Dy^{3+}$ sample

| Data | $Li_3Ba_2Gd_3(WO_4)_8$: 1 at% $Dy^{3+}$ |
|---|---|
| Chemical formula | $Li_3Ba_2Gd_{2.97}Dy_{0.03}(WO_4)_8$ |
| Crystal system | Monoclinic |
| Space group (IT number, $Z$) | $C2/c$ (15, 2) |
| Laue class | $2/m$ |
| Calculated density (g $cm^{-3}$) | 7.4045 |
| Lattice constant $a$, $b$, $c$ (Å) | 5.2126(2), 12.7382(1), 19.1884(3) |
| $\alpha$, $\beta$, $\gamma$ (deg.) | 90, 91.8906(9), 90 |
| Volume ($Å^3$) | 1273.40(4) |
| $2\theta$ range (deg.) | 5–80 |
| $2\theta$ step (deg.) | 0.02 |
| Radiations | Cu K$\alpha$1 ($\lambda$ = 1.5418 Å) |
| Refinement software | GSAS II |
| Reduced $\chi^2$ | 2.25 |
| Goodness of fit (GOF) | 1.50 |
| $R_w$ (%) | 8.092 |

Rietveld refinement was performed for the sample $Li_3Ba_2Gd_3(WO_4)_8$: 1 at% $Dy^{3+}$. The results of the fitting are displayed in Fig. 2. The refinement parameters are listed in Table 1. The crystal structure of $Nd:Li_3Ba_2Y_3(WO_4)_8$ (ref. 29) was taken as a starting model for refinement. The calculated profiles are in good agreement with the experimental profiles. For $Li_3Ba_2Gd_3(WO_4)_8$: 1 at% $Dy^{3+}$, the determined lattice parameters are $a = 5.2126(2)$ Å, $b = 12.7382(1)$ Å, $c = 19.1884(3)$ Å, unit cell volume $V_{calc} = 1273.40(4)$ $Å^3$, monoclinic angle $\beta = a \times c = 91.890(9)°$, and theoretical crystal density $\rho_{calc} = 7.404$ g $cm^{-3}$ (the number of formula units $Z = 2$). The $R_w$ factor was 8.092% and the reduced chi-square value $\chi^2 = 2.25$ showing good convergence of the fit.

The atomic coordinates, sites, occupancy factors (O. F.) and isotropic displacement parameters ($B_{iso}$) obtained for the $Li_3Ba_2Gd_3(WO_4)_8$: 1 at% $Dy^{3+}$ sample are summarized in Table 2. From the results of the Rietveld refinement, a fragment of the $Li_3Ba_2Gd_3(WO_4)_8:Dy^{3+}$ structure in projection on the two crystallographic planes $b$–$c$ and $a$–$b$ was drawn, as shown in Fig. 3. The metal–oxygen (M–O) interatomic distances in the $[Gd|Li1|Dy]O_8$, $[Li2]O_6$, and $[Ba]O_{10}$ polyhedra determined by VESTA analysis of the .cif file are shown in Table 3 and plotted in Fig. 4. $Ba^{2+}$ cations are coordinated with 10 oxygen atoms to form the distorted $[Ba]O_{10}$ polyhedra in which the interatomic distances are determinated to be between 2.6878(1) and 3.0371(5) Å. $Li^+$ ions are located in two crystallographic sites, one called Li2 where the are atoms located in a special crystallographic position with the 4th Wyckoff symbol coordinated by 6 oxygen atoms, and the other called Li1 statistically distributed with $Gd^{3+}|Dy^{3+}$ ions. Each Gd|Li1|Dy is coordinated by eight oxygen atoms to form a distorted polyhedron, the interatomic distances Gd|Li1|Dy–O vary between 2.1345(1) and 2.6146(5) Å. This structure contains $[Gd|Li1|Dy]O_8$, $[Li2]O_6$ and $[Ba]O_{10}$ polyhedra which are further interconnected by sharing oxygen atoms. The nearby $[Gd|Li1|Dy]O_8$ polyhedron leading to a 2-dimensional layered structure parallel to ($b$–$c$) plan. $[Ba]O_{10}$ polyhedron are connected to the adjacent $[Gd|Li1|Dy]O_8$–$[Gd|Li1|Dy]O_8$ layer to form a three-dimensional (3D) network, which results in a one-layer polyhedron structure.

## 3.2. Differential thermal analysis

The DTA curves for the $Li_3Ba_2Gd_3(WO_4)_8$: 10 at% $Dy^{3+}$ sample corresponding to the heating and cooling of the sample are presented in Fig. S1.† A single strong and reversible endothermic (on heating) and exothermic (on cooling) effect can be

**Table 2** Atomic coordinates, sites, occupancy factors (O. F.) and isotropic displacement parameters $B_{iso}$ ($Å^2$) for $Li_3Ba_2Gd_3(WO_4)_8$: 1 at% $Dy^{3+}$ sample

| Atoms | Sites | $x/a$ | $y/b$ | $z/c$ | O. F. | $B_{iso}$ ($Å^2$) |
|---|---|---|---|---|---|---|
| W1 | 8f | 0.4887(7) | 0.4403(3) | 0.4052(7) | 1.000 | 1.224(7) |
| W2 | 8f | 0.5013(8) | 0.7437(6) | 0.3510(3) | 1.000 | 0.884(1) |
| Ba | 4e | 1.0000(0) | 0.5318(8) | 0.2500(0) | 1.000 | 1.684(1) |
| Gd|Li1|Dy | 8f | 0.9666(1) | 0.6532(4) | 0.4564(2) | 0.742|0.250|0.008 | 0.779(4) |
| Li2 | 4e | 0.5000(0) | 0.3220(0) | 0.2500(0) | 1.000 | 1.554(2) |
| O1 | 8f | 0.6296(7) | 0.4145(8) | 0.3215(0) | 1.000 | 2.921(1) |
| O2 | 8f | 0.2547(2) | 0.5490(9) | 0.3926(9) | 1.000 | 2.843(7) |
| O3 | 8f | 0.7456(8) | 0.4830(5) | 0.4636(3) | 1.000 | 2.264(1) |
| O4 | 8f | 0.3402(9) | 0.3321(3) | 0.4530(5) | 1.000 | 3.054(9) |
| O5 | 8f | 0.2892(4) | 0.70776(6) | 0.2864(1) | 1.000 | 2.737(5) |
| O6 | 8f | 0.7328(4) | 0.6524(9) | 0.3632(8) | 1.000 | 3.053(4) |
| O7 | 8f | 0.6621(5) | 0.8621(2) | 0.3220(4) | 1.000 | 2.580(5) |
| O8 | 8f | 0.3267(0) | 0.7626(0) | 0.4312(0) | 1.000 | 2.501(2) |
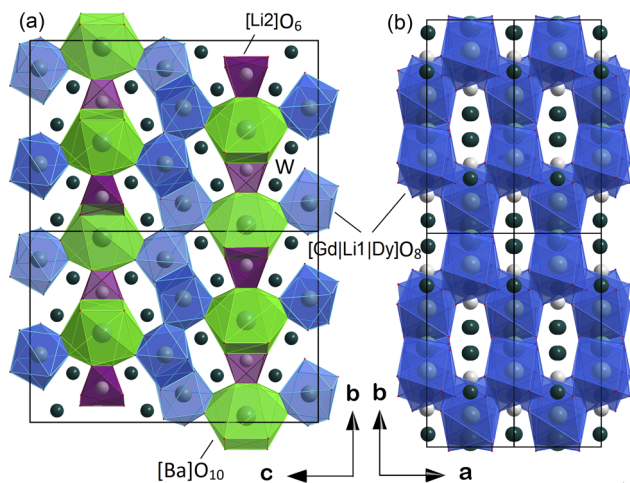
**Fig. 3** Fragment of structure of $Li_3Ba_2Gd_3(WO_4)_8:Dy^{3+}$ in projection to the (a) $b-c$ crystallographic plane and (b) $a-b$ plane.

observed, which corresponds to the congruent melting and crystallization processes. Moreover, the starting temperature of melting corresponds well to 1029 °C, which is a little bit lower than the melting point of the pure host, *i.e.* 1034 °C.[29] Upon cooling the sample, we found an exothermic peak at 1023 °C which could be due to the crystallization of the monoclinic phase. Finally, the absence of additional thermal effects well

reflects the absence of polymorphic phase transformations of the first type below the melting point for this composition.

### 3.3. FTIR & Raman spectroscopy

The FTIR spectra of $Li_3Ba_2Gd_{3-x}(WO_4)_8:xDy^{3+}$ with $0 \le x \le 10$ at% phosphors were recorded and presented in Fig. S2(a),† and they indicate that there is no significant change in the FTIR spectra with increasing $Dy^{3+}$ concentrations. Several intense and sharp peaks can be observed in the range of 400–1500 cm$^{-1}$ which belong to the characteristic absorption of $WO_4^{2-}$. Precursor and calcined samples show absorption peaks corresponding to the appearance of $(WO_4)^{2-}$ groups between 400 and 1000 cm$^{-1}$.[35,36] Among them, the intense absorption bands around 682, 756 and 783 cm$^{-1}$ originate from the double-bridge stretching mode (WOOW). While the least intense peak located at 918 cm$^{-1}$ can be attributed to the band stretching mode (W–O). The peaks at 829 and 423 cm$^{-1}$ are attributed to the band stretching and bending (WOW) modes, respectively.[36] The Raman spectra of $Li_3Ba_2Gd_3(WO_4)_8:xDy^{3+}$ with $x = 0, 1, 3, 5, 7$ and 10 at% measured between 100 and 1000 cm$^{-1}$ under ambient conditions are shown in Fig. S2(b).† Nine modes are observed, the modes centred at 913, and 886 cm$^{-1}$ are assigned to the symmetric stretching of the $(WO_4)^{2-}$ tetrahedra, the modes 840, 795 and 747 cm$^{-1}$ to the asymmetric stretching, the one at 395 cm$^{-1}$ to the asymmetric bending of $WO_4$, the one at 325 cm$^{-1}$ to the symmetrical bending, and the ones at 212 and 128 cm$^{-1}$ to lattice modes.[37–39]

**Table 3** Selected interatomic distances for the polyhedra $[Gd|Li1|Dy]O_8$, $[Li2]O_6$ and $[Ba]O_{10}$ in $Li_3Ba_2Gd_3(WO_4)_8$: 1 at% $Dy^{3+}$

| M–O distances (Å) × numbers | | |
| --- | --- | --- |
| $[Gd|Li1|Dy]O_8$ | $[Li2]O_6$ | $[Ba]O_{10}$ |
| Gd|Li1|Dy–O | Li2–O | Ba–O |
| Gd|Li1|Dy–O6 = 2.1345(1) × 1 | Li2–O1 = 1.9154(3) × 2 | Ba–O7 = 2.6878(1) × 2 |
| Gd|Li1|Dy–O4 = 2.3721(6) × 1 | Li2–O5 = 2.1930(5) × 2 | Ba–O5 = 2.7768(9) × 2 |
| Gd|Li1|Dy–O2 = 2.3896(2) × 1 | Li2–O7 = 2.3310(9) × 2 | Ba–O1 = 2.8312(7) × 2 |
| Gd|Li1|Dy–O8 = 2.4021(6) × 1 | | Ba–O2 = 3.0112(7) × 2 |
| Gd|Li1|Dy–O4′ = 2.4078(6) × 1 | | Ba–O6 = 3.0371(5) × 2 |
| Gd|Li1|Dy–O3 = 2.4603(7) × 1 | | |
| Gd|Li1|Dy–O3′ = 2.4646(7) × 1 | | |
| Gd|Li1|Dy–O8′ = 2.6146(5) × 1 | | |
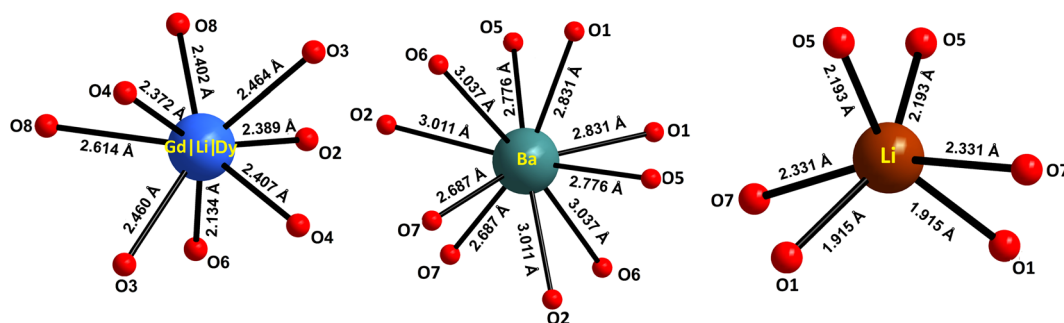


**Fig. 4** Oxygenated environment of $[Gd|Li1|Dy]O_8$, $[Li2]O_6$ and $[Ba]O_{10}$ polyhedra in $Li_3Ba_2Gd_3(WO_4)_8$: 1 at% $Dy^{3+}$. The values indicate the interatomic distances.

## 3.4. Morphology and composition

Fig. 5(a) shows a SEM micrograph of $Li_3Ba_2Gd_{3-x}(WO_4)_8$: 1 at% $Dy^{3+}$ annealed at 900 °C. We observe that the particles have a more or less spherical shape morphology, block-shaped and with a non-uniform size distribution. The composition of the samples studied was determined by line-scan EDX analysis and element mapping. Typical EDX spectra of the Dy-doped sample (with $x = 1$ at%) are shown in Fig. 5(b) and the element mapping of the doped sample is shown in Fig. 5(c). For the Dy-doped sample, we can clearly confirm the presence of Dy as an additional element. The element mapping of Dy and Gd suggests an uniform distribution of the dopant in the host matrix, as also derived from the conclusion of the XRD results.

## 3.5. Bandgap and electronic structure

To gain insight into the electronic structure of $Li_3Ba_2Gd_3(WO_4)_8$, DFT calculations were performed, and the results are shown in Fig. 6(a). The energy gap between the conduction band (CB) minimum and the valence band (VB) maximum was determined

to be 2.45 eV. One can find that the band structure is direct band gap where the maximum of VB and the minimum of CB are located along the same vertical line G. Owing to a relatively large energy gap which can accommodate the ground and excited states of the doped activator, the host was considered to be a suitable matrix for phosphors application. In order to evaluate the experimental optical band gap of the host, diffuse reflectance spectra were recorded in the range of 200–700 nm at room temperature as shown in Fig. 6(b). A broad absorption band with a maximum value at about 300 nm was observed for the undoped sample, this corresponds to the charge transition band (CTB) of oxygen to tungsten $O^{2-} \rightarrow W^{6+}$. The Kubelka–Munk (K–M) relation is employed to evaluate the optical band gap value of the studied host.[40] More details about the K–M calculations could be found in the ESI file.† We plot $[F(R_\infty)h\nu]^2$ as a function of $h\nu$, the bandgap value $E_g$ can be obtained by deducing the fitted regions at the abscissae, as shown in Fig. 6(c). The experimental value of the optical band gap of the host $Li_3Ba_2Gd_3(WO_4)_8$ was found to be equal to 2.79 eV, which is very close to the theoretical one. This underestimation of the theoretical result could be explained by the fact that the Perdew–Burke–Ernzerhof function of the generalized gradient approximation was adopted to deal with exchange correlation interactions.[41,42]

Fig. 7 depicts the total and atom-resolved partial density of states (DOS) of $Li_3Ba_2Gd_3(WO_4)_8$. From the figure we know that the conduction band is caused by the p-state of Ba, the d-state of W and p-state of Gd atoms, while all of the elements contribute to the valence band. The VB with energy stretching from the Fermi energy level around 0 eV to −9.27 eV is mainly caused by the O-2p state and the W-6p, 5d states. The deeper valence band with energy around −20.02 eV is derived from the 5p-state of the Gd atom.

## 3.6. Optical properties

Fig. 8(a) depicts the photoluminescence excitation (PLE) spectra of $Li_3Ba_2Gd_3(WO_4)_8$: 4 at% $Dy^{3+}$ phosphor. There is no difference between the excitation bands under different monitoring wavelengths ($\lambda_{em}$ = 477 and 575 nm), except the excitation intensity. It can be seen that the excitation spectra consist of an intense broad band and some narrow peaks. Among them, the broad excitation band in the UV region from 250 to 310 nm centered at 269 nm is mainly ascribed to the CTB of $WO_4^{2-}$ groups and corresponds to electrons which are excited from the oxygen 2p states to tungsten 5d states through the absorption of photons within the $WO_4^{2-}$ group.[43] The existence of the strong CTB of the $WO_4^{2-}$ group in the excitation spectra indicates the presence of energy transfer from the $WO_4^{2-}$ group to the $Dy^{3+}$ ions in $Li_3Ba_2Gd_3(WO_4)_8$:$Dy^{3+}$ phosphors. It is similar to the previous reported cases for other tungstate phosphors, $NaY(WO_4)_2$:$Dy^{3+}$.[44] In the longer wavelength region from 310 to 500 nm, some sharp lines due to the f–f transitions of $Dy^{3+}$ are observed, which are assigned to the electronic transitions $^6H_{15/2} \rightarrow (^4K_{13/2} + {}^4L_{13/2})$ at 311 nm, $^6H_{15/2} \rightarrow {}^4M_{17/2}$ at 325 nm, $^6H_{15/2} \rightarrow {}^6P_{7/2}$ at 351 nm, $^6H_{15/2} \rightarrow {}^6P_{5/2}$ at 365 nm, $^6H_{15/2} \rightarrow (^4I_{13/2} + {}^4F_{7/2})$ at 386 nm, $^6H_{15/2} \rightarrow {}^4G_{11/2}$ at 427 nm, $^6H_{15/2} \rightarrow {}^4I_{15/2}$ at 453 nm and $^6H_{15/2} \rightarrow {}^4F_{9/2}$ at 475 nm,[45,46] in which there are two
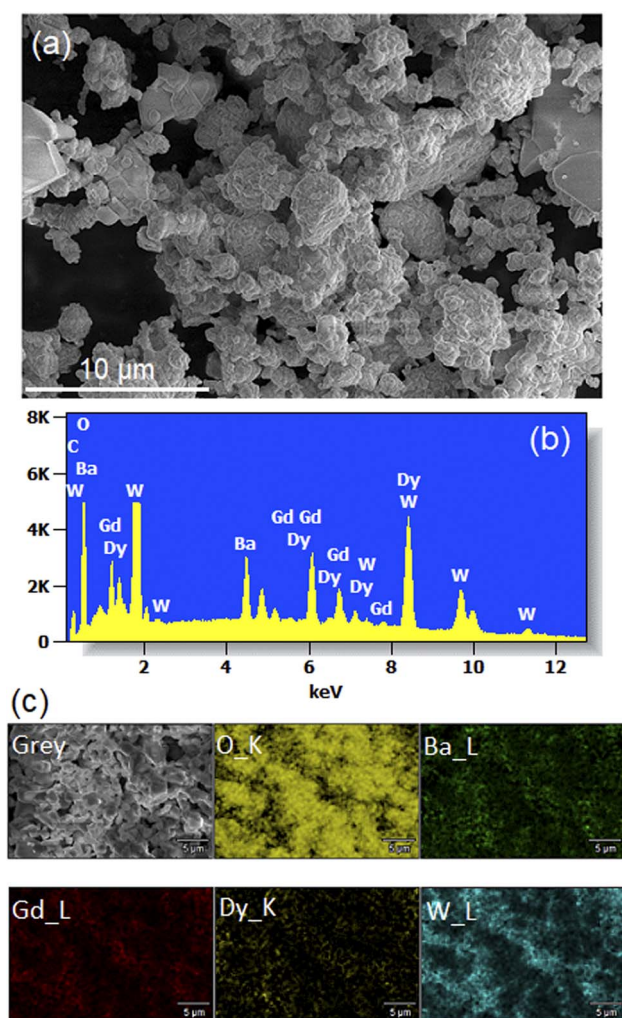


Fig. 5 (a) SEM image (b) Energy-dispersive X-ray (EDX) spectra (c) elemental mapping for the $Li_3Ba_2Gd_3(WO_4)_8$: 1 at% $Dy^{3+}$.

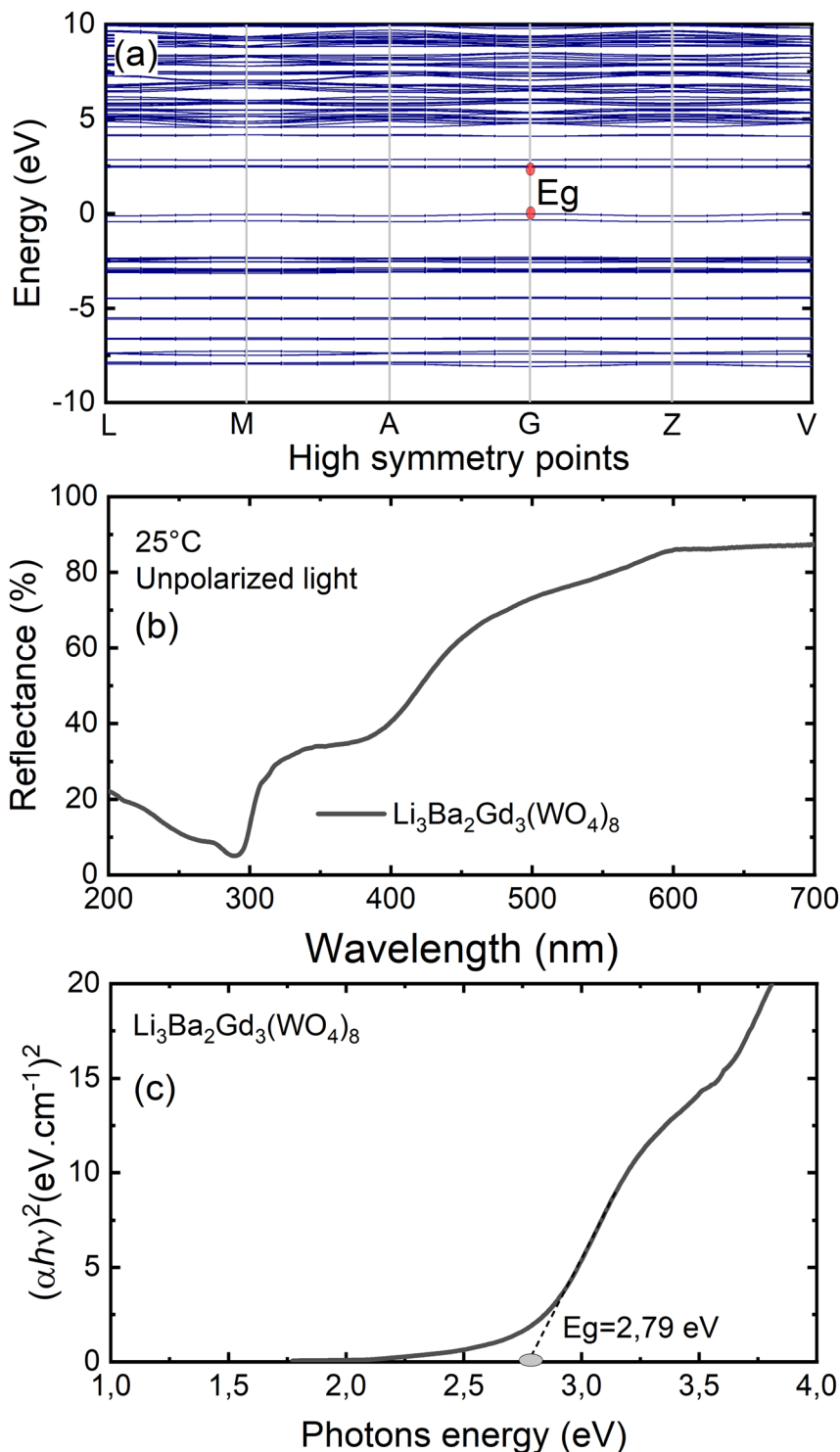**Fig. 6** (a) Results of the DFT calculation on the bandgap structure of $Li_3Ba_2Gd_3(WO_4)_8$; (b) diffuse reflectance spectrum of $Li_3Ba_2Gd_3(WO_4)_8$; (c) Tauc plots to evaluate the optical band gap of $Li_3Ba_2Gd_3(WO_4)_8$, $E_g = 2.79$ eV.

stronger absorption peaks, one in the UV at 350 and the second is in the blue at 450 nm. The intensity of the blue excitation peak is higher with 7.5 nm of excitation bandwidth.

The emission spectra of $Dy^{3+}$ as shown in Fig. 8(b) can be ascribed to the change from excited energy level to a lower energy level. The PL spectra of the phosphors excited at 445 nm

are very similar to those excited at 350 nm. The emission characteristics of the $Dy^{3+}$ doped sample consisted of multiple sharp peaks with multiple wavelengths due to the unique electronic transition in the system. The compact manifolds of energy levels in the upper parts of the activator cause electrons that are excited to decay only through the $^4F_{9/2}$ level to the lower
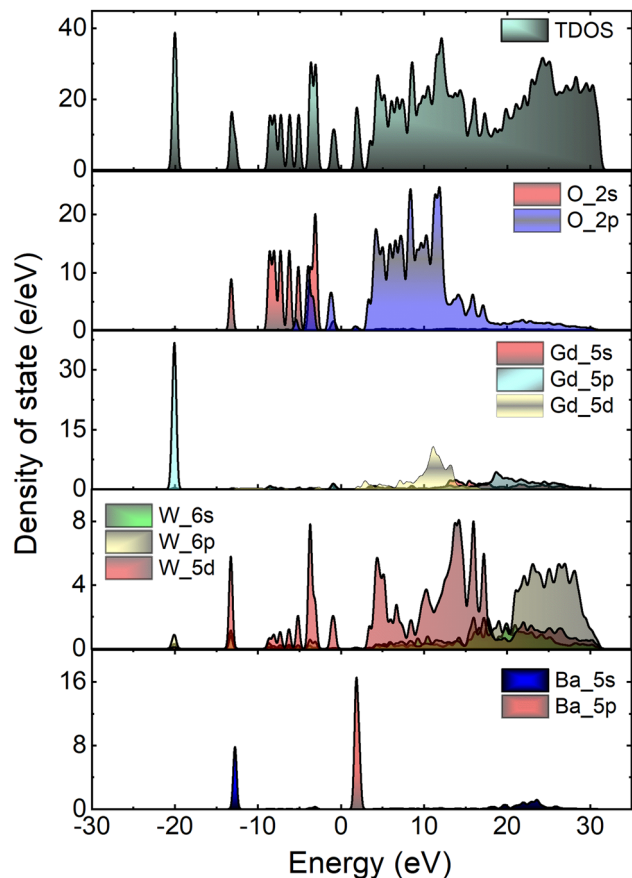
Fig. 7 Calculated total (TDOS) and partial (PDOS) density of states of Li$_3$Ba$_2$Gd$_3$(WO$_4$)$_8$ crystal.

$^6$H$_{j/2}$ ($j$ = 15, 13, 11,9) levels at 477, 575, 661, and 750 nm respectively. The large energy difference between each lower level causes the emission spectra to be separated at a distance. By comparing the emission spectra of the sample Li$_3$Ba$_2$Gd$_3$(-WO$_4$)$_8$: 4 at% Dy$^{3+}$ collected under two different excitation wavelengths, we conclude that the emssion peaks do not change with $\lambda_{ex}$. Furthermore, the ratio Y/B of emission at 575 nm (yellow) and 477 nm (blue), is almost the same for both cases, 5.17. This indicates that in this synthesized series, the predominant color is yellow. That ratio is known to be highly dependent on the site occupied by Dy$^{3+}$. In the compound Li$_3$-Ba$_2$Gd$_3$(WO$_4$)$_8$, the low symmetry of the site occupied by Dy$^{3+}$ increases the 575 nm emission in comparison to the 477 nm emission.[47] Fig. 8(c) shows the energy transfer processes of Dy$^{3+}$ ions in Li$_3$Ba$_2$Gd$_3$(WO$_4$)$_8$: $x$ at% Dy$^{3+}$ phosphors. Under the 350 nm and 445 nm excitation, Dy$^{3+}$ ions absorb the photon energy and transfers it from the ground state $^6$H$_{15/2}$ to the metastable excited states. During this process, the excited populations are rapidly released at the $^4$F$_{9/2}$ energy level by a non-radiative (NR) process that occurs between the excited states. The transitions $^4$F$_{9/2} \rightarrow ^6$H$_{15/2}$, $^4$F$_{9/2} \rightarrow ^6$H$_{13/2}$, $^4$F$_{9/2} \rightarrow$ $^6$H$_{11/2}$ and $^4$F$_{9/2} \rightarrow ^6$H$_{9/2} + ^6$F$_{11/2}$, are radiative and produce the emission peaks at 477, 575, 661 and 750 nm, respectively. Due to the resonance energy between energy levels, the nonradiative energy transfer (ET) and concentration quenching may take

place between $^4$F$_{9/2} + ^6$H$_{15/2}$ and $^6$H$_{15/2} + ^4$F$_{9/2}$, and the cross-relaxation (CR) mechanisms may also take place among neighboring Dy$^{3+}$ ions. Considering the energy match rule, the possible ET and three CR channels are: CR1: $^4$F$_{9/2} + ^6$H$_{15/2} \rightarrow$ $^6$F$_{11/2}$,$^6$H$_{9/2} + ^6$F$_{3/2}$, CR2: $^4$F$_{9/2} + ^6$H$_{15/2} \rightarrow ^6$F$_{9/2}$,$^6$H$_{7/2} + ^6$F$_{5/2}$ and CR3: $^4$F$_{9/2} + ^6$H$_{15/2} \rightarrow ^6$F$_{1/2} + ^6$F$_{11/2}$,$^6$H$_{9/2}$.[44]

Fig. 9(a) shows the concentration of Dy$^{3+}$ ions influences on the PL intensities ofLi$_3$Ba$_2$Gd$_3$(WO$_4$)$_8$: $x$ at% Dy$^{3+}$ phosphor ($x =$ 0.5, 1, 2, 3, 4, 5, 7, and 10) under excitation of 445 nm. The ratio Y/B of the yellow and the blue emission is increased from 4.49 for 0.5 at% sample to 5.58 when the concentration of Dy$^{3+}$ ions is 10 at%. The maximum PL emission intensity was found when the Dy$^{3+}$ doping concentration was 4 at%. Thereafter, the intensity decreases due to concentration-dependent fluorescence quenching. As the concentration of Dy$^{3+}$ doping ions increases, the average distance between Dy$^{3+}$ ions decreases. Cross-relaxation mechanism between adjacent Dy$^{3+}$ ions become more probable. As reported in Fig. 9(b), it is evident that the intensity $^4$F$_{9/2} \rightarrow ^6$H$_{j/2}$ ($j$ = 15, 13, 11, 9) transitions steadily increases with increasing the Dy$^{3+}$ concentration up to 4 at% of Dy$^{3+}$ ions concentration and then quenches for 4 at%. This type of concentration quenching phenomenon can be attributed to the exchange interaction or the multipolar electrical interaction.[48] It is known that when the energy transfer results from the exchange interaction, the critical distance between Dy$^{3+}$ and the quenching site must be less than 4 Å.[49] As suggested by Blasse,[50] the average critical distance of exchange transfer ($R_c$) can be determined as follows:

$$R_c \approx 2\left(\frac{3V}{4\pi \mathcal{X}_c Z}\right)^{\frac{1}{3}},\qquad(2)$$

where $V$ is the volume of the unit cell, $\chi_c$ represents the critical concentration of Dy$^{3+}$ ions, and $Z$ is the number of formula units in the unit cell. For the Li$_3$Ba$_2$Gd$_3$(WO$_4$)$_8$: 4 at% Dy$^{3+}$, $Z =$ 2, $V$ = 1273.40 Å$^3$, and $\chi_c$ = 0.04, the $R_c$ in the Li$_3$Ba$_2$Gd$_3$(-WO$_4$)$_8$:Dy$^{3+}$ phosphors is determined to be 31.209 Å. This value is much larger than 4 Å, revealing that the exchange interaction is not responsible for the energy transfer. The energy transfer between Dy$^{3+}$ ions in Li$_3$Ba$_2$Gd$_3$(WO$_4$)$_8$ phosphors takes place *via* multipole electrical interaction. Different types of multipole interaction such as dipole–dipole (d–d), dipole–quadrupole (d–q) and quadrupole–quadrupole (q–q) interactions are present.[51] In order to determine the type of interaction involved in the energy transfer, Van Uitert[52] proposed an equation:

$$\frac{I}{x} = k\left[1 + \beta(x)^{\frac{\theta}{3}}\right]^{-1},\qquad(3)$$

where $\frac{I}{x}$ represents the emission intensity per activator ($x$), $k$ and $\beta$ are constants for a given host lattice, $\theta$ is the type of interaction between the emitting ions, here $\theta$ = 6, 8, 10 corresponding to dipole–dipole (d–d), dipole–quadrupole (d–q) and quadrupole–quadrupole (q–q) interaction, respectively. Fig. 9(c) shows $I/x$ as a function of $x$ on a logarithmic scale for Li$_3$Ba$_2$Gd$_3$(-WO$_4$)$_8$: $x$ at% Dy$^{3+}$phosphors. The dependence of log$\left(\frac{I}{x}\right)$ on

log($x$) is relatively linear, and the slope ($\theta/3$) is determined to be 2.69. The value of $\theta$ is equal to 8.07, indicating that the concentration quenching in $Li_3Ba_2Gd_3(WO_4)_8$ is attributed to the dipole–quadrupole (d–q) interaction.

To examine the effects of high temperature at real work conditions of wLEDs on the luminescent properties of the prepared $Li_3Ba_2Gd_3(WO_4)_8$: $x$ at% $Dy^{3+}$ luminophores, a series of PL emission spectra in the temperature range of 25–250 °C
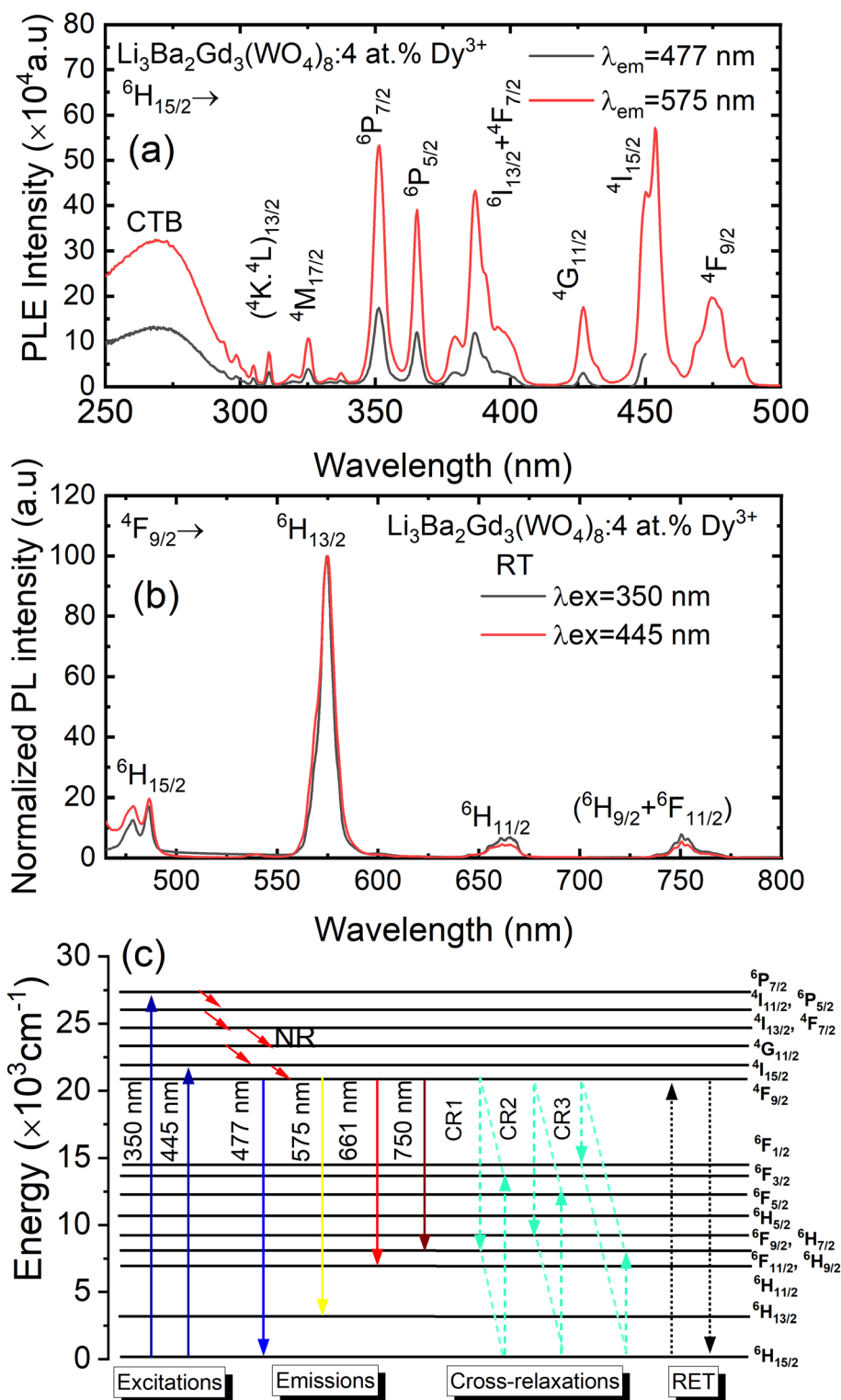


Fig. 8   (a) Excitation spectra of $Li_3Ba_2Gd_3(WO_4)_8$: 4 at% $Dy^{3+}$ phosphor with emission wavelength $\lambda_{em}$ monitored at 477 and at 575 nm; (b) emission spectra under the pumping $\lambda_{ex}$ of 350 nm and 445 nm; (c) schematic energy level diagram showing the excitation and emission mechanism of $Li_3Ba_2Gd_3(WO_4)_8$:$Dy^{3+}$ phosphors (NR = non-radiative transitions; RET = resonance energy transfer).
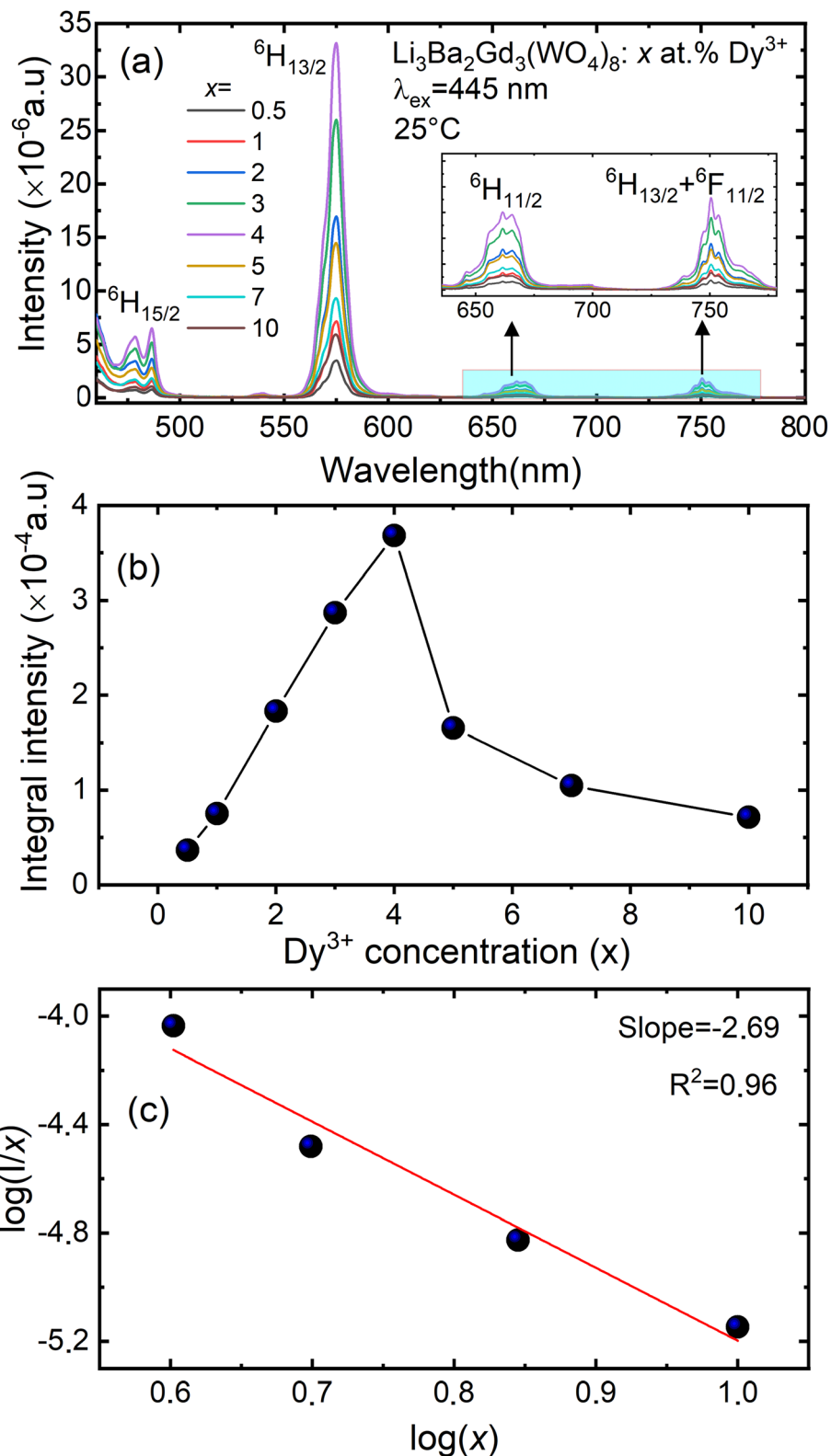
Fig. 9 (a) Emission spectra of $Li_3Ba_2Gd_3(WO_4)_8$: $x$ at% $Dy^{3+}$ (for $x$ = 0.5, 1, 2, 3, 4, 5, 7 and 10); (b) the variation of the integral intensity of the $^4F_{9/2}$ → $^6H_{13/2}$ emission band $vs.$ the $Dy^{3+}$ doping concentration; (c) analysis of the type of interaction by means of the Dexter equation ($x$ – doping concentration of $Dy^{3+}$, $I$ – luminescence intensity).
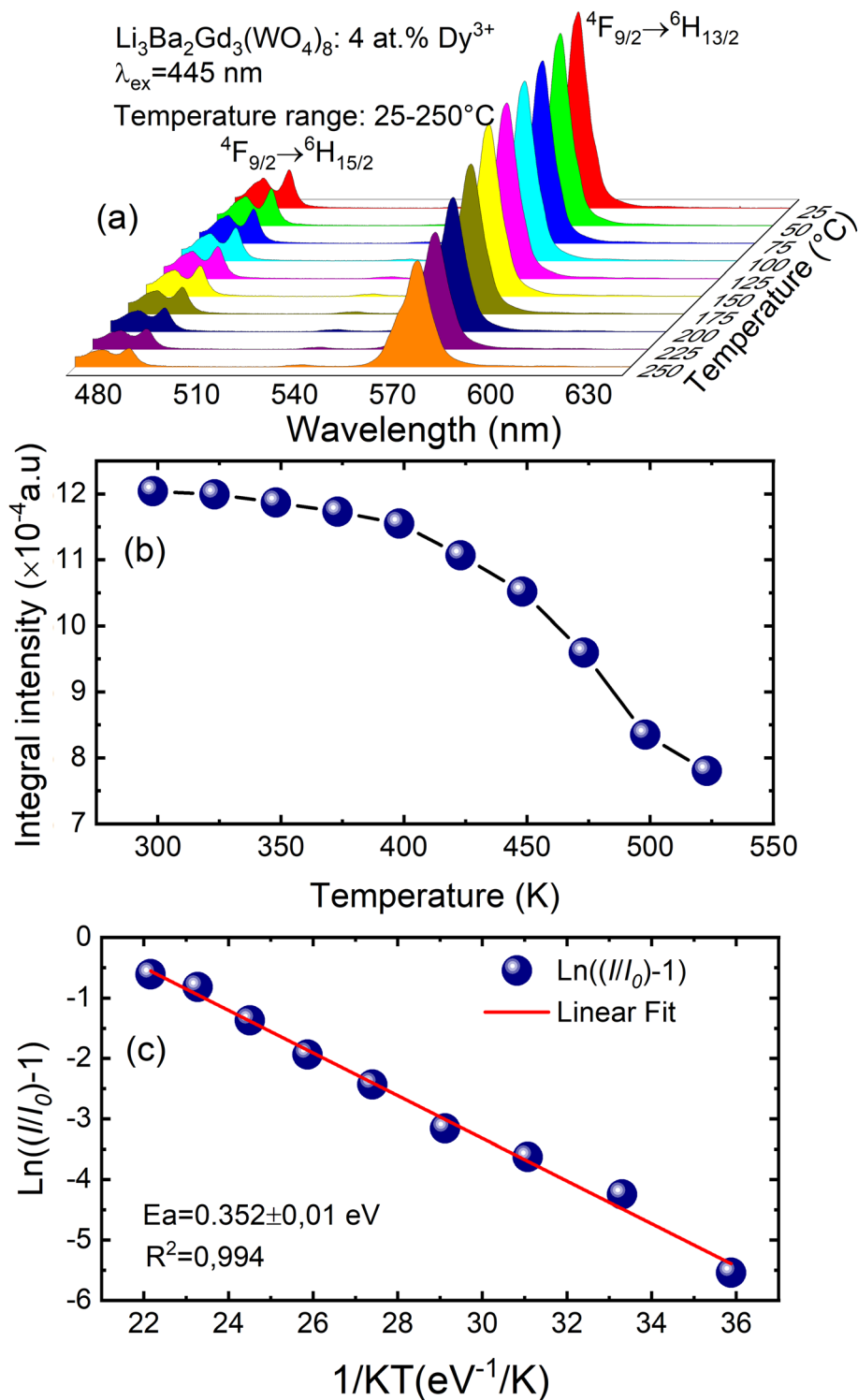
**Fig. 10** (a) Emission spectra of samples doped with 4 at% $Dy^{3+}$ excited at 445 nm under *in situ* temperature ranging from 25 to 250 °C with a step of 25 °C; (b) integral intensity of the $^4F_{9/2} \rightarrow {}^6H_{13/2}$ transition as a function of temperature; (c) $\ln[(I_0/I)-1]$ *vs.* $1/kT$ activation energy graph for thermal quenching of 4 at% $Dy^{3+}$ doped quaternary tungstate $Li_3Ba_2Gd_3(WO_4)_8$.

was acquired for the particular sample with $x = 4$ at% (corresponding to the maximum emission intensity at room temperature), using excitation at 445 nm, see Fig. 10(a). The emission peaks show a similar spectral profile to each other.

The position of the emission peaks does not change with increasing temperature. However, the emission intensities of all peaks gradually decrease with temperature. In the spectra, a double-peaked feature is clearly apparent for the $^4F_{9/2} \rightarrow {}^6H_{15/}$

$_2$ transition from about 488 nm. On the other hand, the samples also do not reach the thermal quenching temperature, indicating high thermal stability at high temperature. Note that the decrease in luminescence intensity with temperature is not monotonic. Thus, at 100 °C the emission intensity is reduced to $\sim$8.5%, at 150 °C it is reduced to $\sim$12.4%, and at 250 °C the integral intensity is around 62% less than of its value at RT, see Fig. 10(b). All $Li_3Ba_2Gd_3(WO_4)_8$ samples doped with $Dy^{3+}$ showed high thermal stability at high temperature. This behavior is attributed to a temperature-induced redistribution of $Dy^{3+}$ ions across the lattice sites. In order to understand the thermal suppression of luminescence of the synthesized materials and to determine the activation energy value of this process, a modified Arrhenius equation was applied:[53]

$$I_T = \frac{I_0}{1 + c \exp\left(-\dfrac{E_a}{KT}\right)}, \tag{4}$$

where $I_0$ and $I_T$ denote the emission intensities of the phosphors at room temperature and at the different temperatures to which the material is subjected, $E_a$ is the activation energy for thermal suppression of the phosphor, $c$ is a pre-exponential factor and $K$ is the Boltzmann constant ($8.617 \times 10^{-5}$ eV $K^{-1}$).[54] The value of $E_a$ can be estimated from the slope of the curve of $\ln[(I_0/I_T) - 1]$ versus $1/KT$ in Fig. 10(c). The data were fitted linearly and the activation energy of thermal suppression was calculated for $Li_3Ba_2Gd_3(WO_4)_8$ phosphors doped with 4 at% $Dy^{3+}$ resulting $0.352 \pm 0.01$ eV. For $Dy^{3+}$, the emission band used to calculate the activation energy was assigned to the $^4F_{9/2} \rightarrow {}^6H_{15/2}$ band. In agreement with the ligand field perturbation (LFP) theory, the distribution is $2J + 1$. On this basis, for $Dy^{3+}$ $2x(15/2) + 1 = 16$ showing that for trivalent $Dy^{3+}$ ions there are 16 splitting states. Based on this information, $Dy^{3+}$ has a high thermal coupling level due to the high number of $2J + 1$ values, while the energy loss by thermal coupling is higher. Therefore, the result is a low activation energy value for $Dy^{3+}$.

In order to determine the color parameters, the CIE coordinates ($x,y$) and the correlated color temperature parameter (CCT) were obtained using the standard formula. The chromaticity coordinates can be calculated from the tri-stimulus values of CIE 1931-XYZ tri-chromatic system,[55,56] more details about this calculation is presented in the ESI file.† CIE chromaticity coordinates are generally used to check the exact emission color and color purity. The emission spectra of $Li_3Ba_2Gd_3(WO_4)_8$: $x$ at% $Dy^{3+}$ phosphors were used to calculate the CIE chromaticity coordinates. The calculated chromaticity for different concentration levels are displayed in Fig. 11 and their numerical values are shown in Table 4. The small shifting in the ($x,y$) coordinates when the concentration of the $Dy^{3+}$ increases is explained by the change of the ratio Y/B mentioned above.

From Fig. 11, it can be seen that all the coordinates are located in the greenish-yellow color region of the CIE diagram, demonstrating that the $Dy^{3+}$-doped $Li_3Ba_2Gd_3(WO_4)_8$ phosphors have potential for white LED applications. The same color found by calculating the CIE chromaticity coordinates, can be seen when we illuminate the sample with blue light at 450 nm, see the inset in Fig. 12. After obtaining the chromaticity
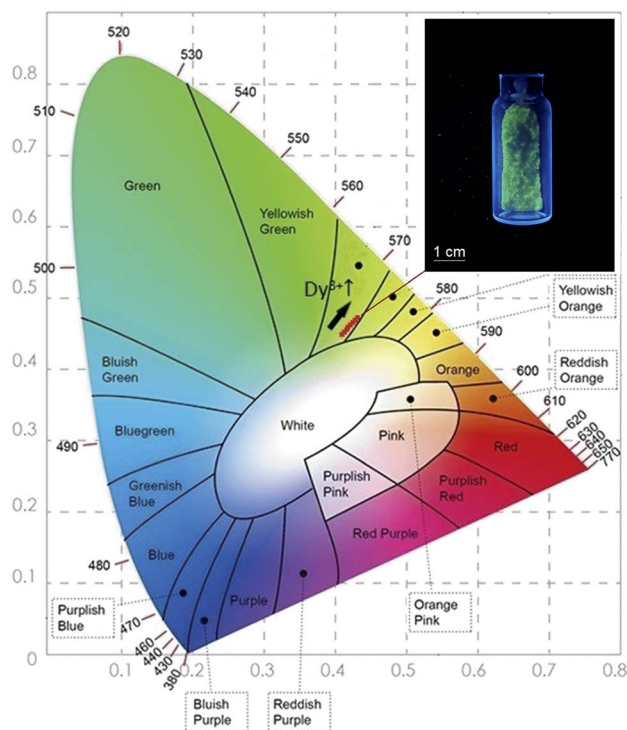


**Fig. 11** The CIE chromaticity diagram of the $Dy^{3+}$ doped $Li_3Ba_2Gd_3(WO_4)_8$ phosphors at 445 nm of Excitation; (inset) a photograph of the greenish-yellow phosphor under blue light illumination.

**Table 4** The CIE coordinates and CCT values for the $Dy^{3+}$ doped $Li_3Ba_2Gd_3(WO_4)_8$ phosphors

| $Dy^{3+}$ concentration (at%) | $x$ | $y$ | CCT (K) | Color purity (%) |
|---|---|---|---|---|
| 0.5 | 0.417 | 0.467 | 3756 | 95 |
| 1 | 0.418 | 0.466 | 3736 | 96.4 |
| 2 | 0.421 | 0.471 | 3701 | 96.8 |
| 3 | 0.424 | 0.471 | 3663 | 97.1 |
| 4 | 0.425 | 0.472 | 3652 | 98 |
| 5 | 0.424 | 0.474 | 3668 | 98.2 |
| 7 | 0.428 | 0.477 | 3619 | 98.5 |
| 10 | 0.430 | 0.481 | 3621 | 98.3 |

coordinates, the CCT can be calculated using the following empirical McCamy formula:[57]

$$CCT = -449n^3 + 3525n^2 - 6823.3n + 5520.33, \tag{5}$$

where $n$ is the anti-slope line, $n = \dfrac{x - x_e}{y - y_e}$, while $x_e$ and $y_e$ correspond to the epicenter, the values of $x_e$ and $y_e$ are 0.332 and 0.186 respectively. The CCT values were calculated as 3756, 3736, 3701, 3663, 3652, 3668, 3619 and 3621 K for the eight synthesized phosphors. The results exhibited the characteristics of low color correlated temperature. The color purity of phosphors is also a key factor in producing a better light source for LED applications.[58] To determine this factor, the following formula is used:
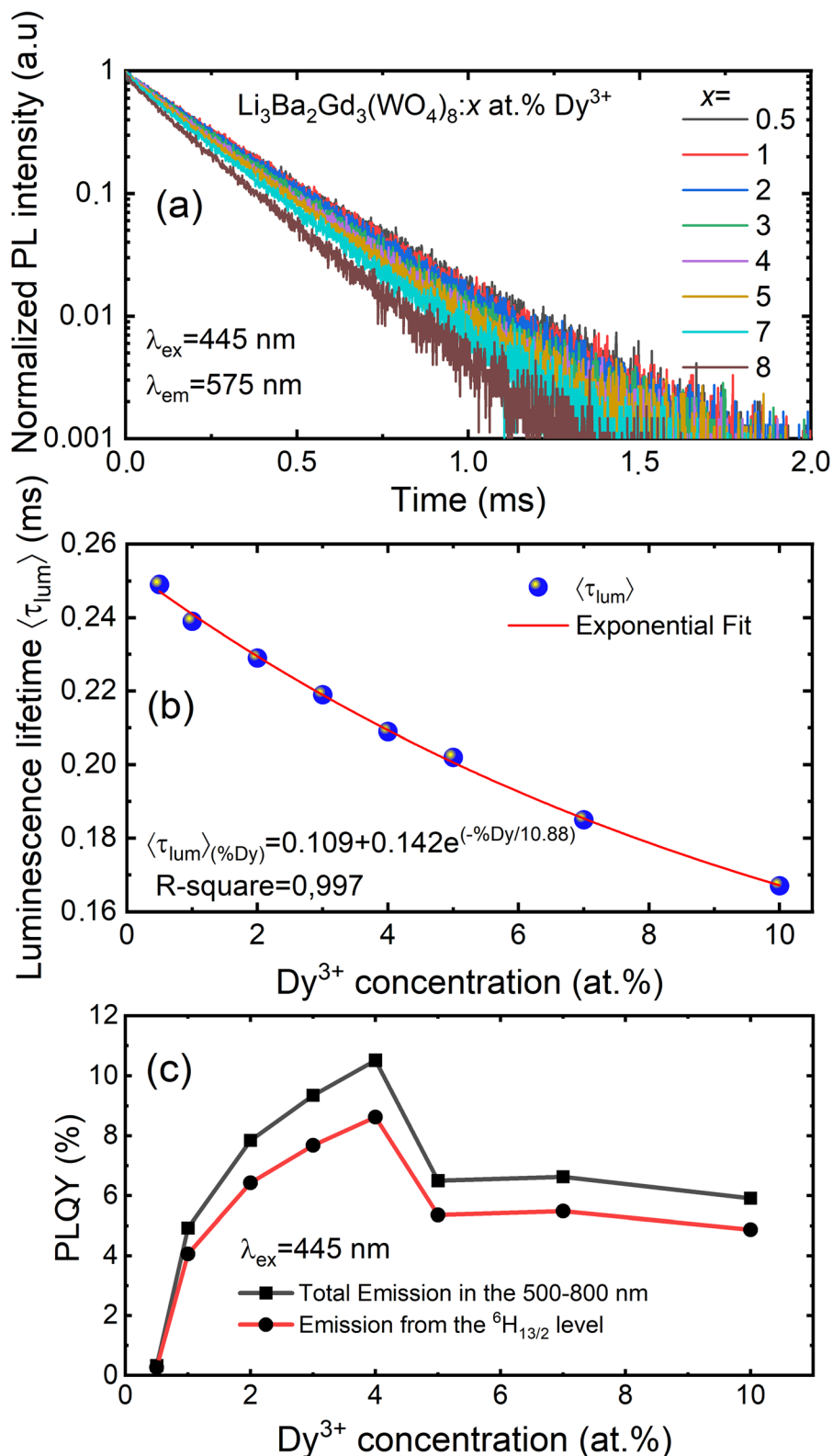
Fig. 12   (a) Decay curves of $Li_3Ba_2Gd_3(WO_4)_8$: $x$ at% $Dy^{3+}$ ($x = 0.5, 1, 2, 3, 4, 5, 7,$ and 10) ($\lambda_{ex} = 445$ nm, $\lambda_{em} = 575$ nm); (b) the exponential fitting of the average decay lifetime as function of concentration level of $Dy^{3+}$ ions; (c) PLQY in the 500–800 nm range and DS PLQY of the $^4F_{9/2} \rightarrow {}^6H_{13/2}$ emission band under 445 nm excitation vs. the $Dy^{3+}$ doping concentration.

**Table 5** Comparison of the emission properties of $Dy^{3+}$-activated yellow-emitted phosphors

| Phosphor | $\lambda_{ex}$ (nm) | $x$ | $y$ | CCT (K) | $\tau_{lum}$ (ms) | PLQY (%) | Ref. |
| --- | --- | --- | --- | --- | --- | --- | --- |
| $Li_3Ba_2Gd_3(WO_4)_8$ | 445 | 0.425 | 0.472 | 3652 | 0.209 | 10.5 | This work |
| $NaLi_9(SiO_4)O_9$ | 445 | 0.469 | 0.495 | 3150 | 0.630 | — | 16 |
| $Sr_3LaNb_3O_{12}$ | 352 | 0.425 | 0.450 | 3252 | — | 18.24 | 60 |
| $Ca_3TeO_6$ | 349 | 0.417 | 0.461 | 3735 | 0.506 | — | 61 |
| $NaLa(MoO_4)_2$ | 352 | 0.345 | 0.386 | — | 0.150 | 22 | 62 |
| $(Ca,Sr)_7(SiO_3)_6Cl_2$ | 380 | 0.350 | 0.502 | — | — | 24.6 | 63 |
| $NaLaMgWO_6$ | 388 | 0.441 | 0.475 | — | 0.133 | 15.8 | 17 |
| $SrAl_2O_4$ | 350 | 0.300 | 0.345 | — | 0.930 | 9.52 | 64 |

$$\text{color purity} = \frac{\sqrt{(x - x_e)^2 + (y - y_e)^2}}{\sqrt{(x_d - x_e)^2 + (y_d - y_e)^2}} \times 100\%, \qquad (6)$$

where $(x, y)$, $(x_e, y_e)$ and $(x_d, y_d)$ are the chromaticity coordinates of the sample point, the equal energy point (0.33, 0.33) and the dominant wavelength point, respectively. The dominant wavelength point can be calculated based on the intersection point of the connection line between the sample point and the equal energy point. For the sample with the highest emission intensity ($x = 4$ at%), the chromaticity coordinates are (0.4251, 0.4722) corresponding to a dominant wavelength of 575 nm located in the yellow range with a color purity of 98%. When we increase the level of $Dy^{3+}$ doping, we see a tendency to shift the $(x, y)$ coordinates towards the green emission and increase the color purity.

The luminescence decay curves of $Li_3Ba_2Gd_3(WO_4)_8$: $x$ at% $Dy^{3+}$ phosphors at RT are shown in Fig. 12(a), ($\lambda_{ex} = 445$ nm and $\lambda_{em} = 575$ nm). The decay process can be well fitted by single exponential function the eqn (7) as follows:

$$\langle \tau_{lum} \rangle = \frac{\int_0^\infty t \times I_{(t)} dt}{\int_0^\infty I_{(t)} dt}, \qquad (7)$$

where $I(t)$ is the PL intensity at time $t$ subsequently to excitation, $\langle \tau_{lum} \rangle$ is the average decay times. The average lifetime of $Dy^{3+}$:$^4F_{9/2}$ level in $Li_3Ba_2Gd_3(WO_4)_8$: $x$ at% $Dy^3$ ($x = 0.5, 1, 2, 3, 4, 5, 7$ and 10) samples are 0.249, 0.239, 0.229, 0.219, 0.209, 0.202, 0.185 and 0.167 ms, respectively. The decay time of $Dy^{3+}$ obviously decreases with increasing concentration, which means non-radiative transitions increase. The trend of decay lifetime of the phosphors against the doping concentration can be well fitted with the single-exponential equation $y = 0.109 + 0.142 \exp(-x/10.88)$, as shown in Fig. 12(b).

By monitoring within the luminescence range of 500–800 nm and excited with 445 nm blue radiation, the absolute photoluminescence quantum yield, PLQY was obtained for different concenrtaion levels of $Dy^{3+}$ ions. It was directly measured using a QE Pro-Ocean Insight spectrofluorimeter with an integrating sphere. The PLQY can be calculated as follows[59]: PLQY = $L_S/(E_R - E_S)$, where $L_S$ is the integrated intensity of the luminescence emission spectrum of the sample, $E_S$ is the integrated intensity of the spectrum of light used for exciting the sample, and $E_R$ is the integrated intensity of the spectrum of excitation light without the sample in the sphere. The result of the calculation

are shown in Fig. 12(c). We can see that the doping concentration of $Dy^{3+}$ ion has a great impact on the PLQY. The value for the sample with the strongest emission, 4 at% $Dy^{3+}$, was found to be 10.5%. However, the PLQY of $Li_3Ba_2Gd_3(WO_4)_8$:$Dy^{3+}$ can be enhanced by controlling the particle size, size distribution, morphology, and crystalline defects through optimization of the processing conditions and composition. Hence, $Li_3Ba_2-Gd_3(WO_4)_8$:$Dy^{3+}$ can be a good candidate for the yellow component applied in wLEDs.

Table 5 provides a comparative view of the emission properties of several yellow-emitted $Dy^{3+}$-activated inorganic phosphors materials studied so far. The chromatic coordinates $(x,y)$ of the yellow emission vary from material to another, depending on the actual composition of the host phosphor and the excitation wavelength. In our case, the yellow/blue emission ratio (Y/B) under 445 nm-blue excitation is relatively high compared to other phosphors, resulting in a strong greenish-yellow luminescence.

## 4. Conclusions

New quaternary tungstate $Li_3Ba_2Gd_3(WO_4)_8$:$Dy^{3+}$ phosphors were successfully synthesized by the solid-state reaction, and its microstructural, spectroscopic and opticals properties were investigated in detail. X-ray diffraction Rietveld analysis revealed that the prepared luminophores crystallize in the monoclinic system with the $C2/c$ space group and that the dopant ions $Dy^{3+}$ replace the cations $Gd^{3+}$ occupying the crystallographic site 8f. The FE-SEM micrograph revealed that the as-synthesized powder particles had micron size with irregular shape. The DFT calculations for the undoped sample showed a direct band gap of 2.45 eV. The excitation spectra indicated that this phosphor could be effectively excited with blue laser diode emitting at 445 nm. The PL spectra of the luminophores are dominated by the $^4F_{9/2} \rightarrow {}^6H_{13/2}$ band at 575 nm that determines a strong greenish-yellow emission color. The optimum concentration of $Dy^{3+}$ is 4 at%, and the dipole-quadrupole is the dominant mechanism for concentration quenching. The decay curves were single exponential in nature and the decay time value decreases with increasing $Dy^{3+}$ ion concentration, which suggests energy transfer between adjacent $Dy^{3+}$ ions. The absolute photoluminescence quantum yield was found to be stronlgly dependent on the concentration of $Dy^{3+}$ ions and its 10.5% for the sample with the strongest emission.

The temperature dependent PL revealed good thermal stability of the as-synthesized phosphor with an appreciable activation energy of 0.352 eV. The combination of the findings mentioned above suggests the prospective utility of the synthesized phosphors for applications in wLEDs under the excitation of blue LED chips.

## Conflicts of interest

There are no conflicts to declare.

## Acknowledgements

## References

1 H. Guo, X. Wang, J. Chen and F. Li, *Opt. Mater. Express*, 2010, **18**, 1513–1515.

2 W. Yang, C. Liu, S. Lu, J. Du, Q. Gao, R. Zhang, Y. Liu and C. Yang, *J. Mater. Chem. C*, 2018, **6**, 290–298.

3 H. Li, H. M. Noh, B. K. Moon, B. C. Choi, J. H. Jeong, K. Jang, H. S. Lee and S. S. Yi, *Inorg. Chem.*, 2013, **52**, 11210–11217.

4 W. Lu, N. Guo, Y. Jia, Q. Zhao, W. Lv, M. Jiao, B. Shao and H. You, *Inorg. Chem.*, 2013, **52**, 3007–3012.

5 H. Guo and X. Huang, *J. Alloys Compd.*, 2018, **764**, 809–814.

6 V. Bachmann, C. Ronda and A. Meijerink, *Chem. Mater.*, 2009, **21**, 2077–2084.

7 R. Zhang, T. Maeda, R. Maruta, S. Kusaka, B. Ding, K.-I. Murai and T. Moriga, *J. Solid State Chem.*, 2010, **183**, 620–623.

8 W. Li, G. Fang, Y. Wang, Z. You, J. Li, Z. Zhu, C. Tu, Y. Xu and W. Jie, *Vacuum*, 2021, **188**, 110215.

9 V. J. Fratello and C. D. Brandle, *J. Cryst. Growth*, 1993, **128**, 1006–1010.

10 L. Zhao, F. Fan, X. Chen, Y. Wang, Y. Li and B. Deng, *J. Mater. Sci.: Mater. Electron.*, 2018, **29**, 5975–5981.

11 F. Fan, L. Zhao, Y. Shang, J. Liu, W. Chen and Y. Li, *J. Lumin.*, 2019, **211**, 14–19.

12 H. Chen, P. Loiseau and G. Aka, *J. Lumin.*, 2018, **199**, 509–515.

13 H. Liu, L. Liao, Q. Guo, D. Yang and L. Mei, *J. Lumin.*, 2017, **181**, 407–410.

14 R. Mi, J. Chen, Y. Liu, L. Mei, J. Yuan, Y. Xia, Z. Huang and M. Fang, *Mater. Res. Bull.*, 2017, **86**, 146–152.

15 Q. Liu, J. Guo, M. Fan, Q. Zhang, S. Liu, K. L. Wong, Z. Liu and B. Wei, *J. Mater. Chem. C*, 2020, **8**, 2117–2122.

16 S. Slimi, P. Loiko, K. Bogdanov, A. Volokitina, R. M. Solé, M. Aguiló, F. Díaz, E. Ben Salem and X. Mateos, *J. Alloys Compd.*, 2022, **896**, 163109.

17 B. Han, Y. Dai, J. Zhang and H. Shi, *Mater. Lett.*, 2017, **204**, 145–148.

18 Y. Wei, C. Tu, H. Wang, F. Yang, G. Jia, Z. You, X. Lu, J. Li, Z. Zhu and Y. Wang, *J. Alloys Compd.*, 2007, **438**, 310–316.

19 W. W. Zhou, B. Wei, W. Zhao, G. F. Wang, X. Bao, Y. H. Chen, F. W. Wang, J. M. Du and H. J. Yu, *Opt. Mater.*, 2011, **34**, 56–60.

20 W. Zhao, W. W. Zhou, B. Wei, Y. Yu, G. F. Wang, J. M. Du, H. J. Yu, Z. C. Lv and Y. H. Chen, *J. Alloys Compd.*, 2012, **538**, 136–143.

21 Y. C. Chang, C. H. Liang, S. A. Yan and Y. S. Chang, *J. Phys. Chem. C*, 2010, **114**, 3645–3652.

22 M. Shang, G. Li, X. Kang, D. Yang and J. Lin, *J. Electrochem. Soc.*, 2011, **158**, H565.

23 K. Subbotin, P. Loiko, S. Slimi, A. Volokitina, A. Titov, D. Lis, E. Chernova, S. Kuznetsov, R. M. Solé, U. Griebner, V. Petrov, M. Aguiló, F. Díaz, P. Camy, E. Zharikov and X. Mateos, *J. Lumin.*, 2020, **228**, 117601.

24 Y. Pan, Y. Chen, Y. Lin, X. Gong, J. Huang, Z. Luo and Y. Huang, *CrystEngComm*, 2012, **14**, 3930–3935.

25 G. Q. Wang, X. H. Gong, Y. J. Chen, J. H. Huang, Y. F. Lin, Z. D. Luo and Y. D. Huang, *Opt. Mater.*, 2014, **36**, 1255–1259.

26 B. Xiao, Z. Lin, L. Zhang, Y. Huang and G. Wang, *PLoS One*, 2012, **7**, 40631.

27 W. Guo, Y. Tian, P. Huang, L. Wang, Q. Shi and C. Cui, *Ceram. Int.*, 2016, **42**, 5427–5432.

28 J. Hu, X. Gong, J. Huang, Y. Chen, Y. Lin, Z. Luo and Y. Huang, *Opt. Mater. Express*, 2016, **6**, 181.

29 H. Li, L. Zhang and G. Wang, *J. Alloys Compd.*, 2009, **478**, 484–488.

30 Y. Zhao, Y. Huang, L. Zhang, Z. Lin and G. Wang, *Optoelectron. Adv. Mater., Rapid Commun.*, 2012, **6**, 357–362.

31 W. L. Guo, Y. T. Jiao, P. S. Wang, Q. Liu, S. Liu and F. Hou, *Solid State Phenom.*, 2018, **281**, 686–691.

32 S. J. Clark, M. D. Segall, C. J. Pickard, P. J. Hasnip, M. I. J. Probert, K. Refson and M. C. Payne, *Z. Kristallogr.*, 2005, **220**, 567–570.

33 R. D. Shannon, *Acta Crystallogr.*, 1976, **32**, 751–767.

34 Y. Han, S. Wang, H. Liu, L. Shi, A. Song, X. Lu, J. Wei, Z. Mao, D. Wang, Z. Mu, Z. Zhang and S. Niu, *J. Alloys Compd.*, 2020, **844**, 156070.

35 S. P. S. Porto and J. F. Scott, *Phys. Rev.*, 1967, **157**, 716–719.

36 L. Macalik, J. Hanuza and A. A. Kaminskii, *J. Raman Spectrosc.*, 2002, **33**, 92–103.

37 P. Tarte and M. Liegeois-Duyckaerts, *Spectrochim. Acta, Part A*, 1972, **28**, 2029–2036.

38 J. Hanuza, A. Haznar, M. A. Pietraszko, A. Lemiec, J. H. Van Der Maas3, M. Czka and E. T. G. Lutz3, *J. Raman Spectrosc.*, 1997, **28**, 953–963.

39 J. Hanuza and L. Macalik, *Spectrochim. Acta, Part A*, 1987, **43**, 361–373.

40 A. S. Rajashekharaiah, G. P. Darshan, R. B. Basavaraj, Y. V. Naik, D. Kavyashree, S. C. Sharma and H. Nagabhushana, *Opt. Mater.*, 2019, **95**, 109237.

41 J. P. Perdew, K. Burke and M. Ernzerhof, *Phys. Rev. Lett.*, 1996, **77**, 3865–3868.

42 V. N. Staroverov, G. E. Scuseria, J. P. Perdew, E. R. Davidson and J. Katriel, *Phys. Rev. A: At., Mol., Opt. Phys.*, 2006, **74**, 1–4.

43 C. A. Kodaira, H. F. Brito and M. C. F. C. Felinto, *J. Solid State Chem.*, 2003, **171**, 401–407.

44 X. Liu, W. Xiang, F. Chen, Z. Hu and W. Zhang, *Mater. Res. Bull.*, 2013, **48**, 281–285.

45 J. Wang, Y. Xu, M. Hojamberdiev, Y. Cui, H. Liu and G. Zhu, *J. Alloys Compd.*, 2009, **479**, 772–776.

46 G. Jia, Y. Song, M. Yang, Y. Huang, L. Zhang and H. You, *Opt. Mater.*, 2009, **31**, 1032–1037.

47 J. Zhang, Z. Yu, J. Guo, W. Yan and W. Xue, *J. Alloys Compd.*, 2017, **703**, 156–162.

48 J. S. Kim, P. E. Jeon, Y. H. Park, J. C. Choi, H. L. Park, G. C. Kim and T. W. Kim, *Appl. Phys. Lett.*, 2004, **85**, 3696–3698.

49 Y. Zhang, D. Geng, M. Shang, X. Zhang, X. Li, Z. Cheng, H. Lian and J. Lin, *Dalton Trans.*, 2013, **42**, 4799–4808.

50 G. Blasse, *Phys. Lett. A*, 1968, **28**, 444–445.

51 P. B. Devaraja, D. N. Avadhani, H. Nagabhushana, S. C. Prashantha, S. C. Sharma, B. M. Nagabhushana, H. P. Nagaswarupa and B. Dharuka Prasad, *Mater. Charact.*, 2014, **97**, 27–36.

52 D. L. Dexter and J. H. Schulman, *J. Chem. Phys.*, 1954, **22**, 1063–1070.

53 J. Zhou, Z. Xia, M. Yang and K. Shen, *J. Mater. Chem.*, 2012, **22**, 21935–21941.

54 C. D. S. Brites, P. P. Lima, N. J. O. Silva, A. Millán, V. S. Amaral, F. Palacio and L. D. Carlos, *New J. Chem.*, 2011, **35**, 1177–1183.

55 K. V. Krishnaiah, K. U. Kumar and C. K. Jayasankar, *Mater. Express*, 2013, **3**, 61–70.

56 B. Shanmugavelu and V. V. R. K. Kumar, *J. Lumin.*, 2014, **146**, 358–363.

57 I. E. Ashdown, *Proceeding of the SPIE, Solid State Lighting II*, 2002, vol. 4776, p. 51.

58 Y. J. Yun, J. K. Kim, J. Y. Ju, S. K. Choi, W. I. Park, J. Y. Suh, H. K. Jung, Y. Kim and S. Choi, *Phys. Chem. Chem. Phys.*, 2017, **19**, 11111–11119.

59 Z. Xia, J. Zhuang and L. Liao, *Inorg. Chem.*, 2012, **51**, 7202–7209.

60 Y. Zhang, Z. Liang, W. Wang, Y. Lin, R. Tang, J. Wang, D. He, J. Liu, Z. Zhang, L. Zhao, B. Deng, D. Zhang and R. Yu, *J. Mater. Sci.: Mater. Electron.*, 2022, **33**, 26619–26632.

61 G. Zhang, L. Zhao, F. Fan, Y. Bai, B. Ouyang, W. Chen, Y. Li and L. Huang, *Spectrochim. Acta, Part A*, 2019, **223**, 117343.

62 H.-N. Huang, J. Zhou, H.-F. Zhou, Z.-C. Yu, Y.-Q. Wu and G.-J. Zhou, *J. Nanosci. Nanotechnol.*, 2018, **18**, 5433–5440.

63 F. Liu, Y. Fang, N. Zhang, J. Hou, L. Zhang, S. Yu and S. Liu, *J. Rare Earths*, 2014, **32**, 812–816.

64 B. C. Jamalaiah and Y. Ramesh Babu, *Mater. Chem. Phys.*, 2018, **211**, 181–191.